Characterization of the transitional zone between fully carbonated and non-carbonated areas in slag-rich cement paste after long-term natural exposure

Zhang, Yu; He, Shan; Liang, Xuhui; Liang, Minfei; Çopuroğlu, Oğuzhan; Schlangen, Erik

DOI
10.1016/j.cemconres.2025.107986

Publication date
2025

Document Version
Final published version

Published in
Cement and Concrete Research

Cement and Concrete Research 198 (2025) 107986

Contents lists available at ScienceDirect

Cement and Concrete Research

journal homepage: www.elsevier.com/locate/cemconres

Characterization of the transitional zone between fully carbonated and non-carbonated areas in slag-rich cement paste after long-term natural exposure

Yu Zhang [a,b], Shan He [b,*], Xuhui Liang [b], Minfei Liang [b,c], Oğuzhan Çopuroğlu [b], Erik Schlangen [b]

[a] Key Laboratory of Concrete and Prestressed Concrete Structures of the Ministry of Education, Southeast University, Nanjing 210096, China
[b] Microlab, Section Materials and Environment, Faculty of Civil Engineering and Geosciences, Delft University of Technology, Delft 2628 CN, the Netherlands
[c] Clarendon Laboratory, Department of Physics, University of Oxford, Oxford OX1 3PU, United Kingdom

ARTICLE INFO

Keywords:
Transitional zone
Slag-rich cement paste
Natural carbonation
Microstructural-micromechanical-mineralogical properties

ABSTRACT

Due to the gradual diffusion of CO_2 under natural exposure, areas with varied degrees of carbonation exist at different depths from the surface of slag-rich cement paste. While extensive research has been dedicated to investigating the fully carbonated zone as identified by phenolphthalein spray, the transitional zone, located between the fully carbonated and the uncarbonated regions, has received comparatively less attention. This study thus aims to address this research gap by exploring its microstructural, micromechanical, and mineralogical properties. The results reveal that carbonation-induced damage extends beyond the fully carbonated zone as identified by phenolphthalein. Particularly in the transitional area close to the carbonated zone, nano-indentations results reveal that micromechanical properties of this area are even lower to that of the fully carbonated zone. In addition, mineralogical investigation suggest that the depth of carbonation stays within the range where slag-containing blends loses its green coloration. By comparing specimens with different slag composition, it was found that the depth of this faded green area can be an important indicator to assess the carbonation resistance of slag-containing blends.

1. Introduction

Blast furnace slag (henceforth *slag*) is the by-product of pig iron production [1], and it is one of the most used supplementary cementitious materials (SCMs) in cement and concrete industry [2,3]. Due to the formation of a denser microstructure, concretes adopted slag cement are less prone to deteriorations such as alkali silica reaction, sulfate attack, and chloride ingress [4–6]. An exception is carbonation, which renders a poor microstructure at the skin area of slag-rich concretes [7,8] owing to the reduced portlandite content after hydration [9,10].

The carbonation of cementitious materials is a neutralization process, in which CO_2 from the atmosphere penetrates into the cement-based matrix and reacts with the alkaline species in the pore solution, leading to the reduction of alkalinity (*i.e.*, pH) and the modification of phase assemblage [7,8,11,12]. As blended cements commonly contain lower calcium hydroxide content, the carbonation rate of slag cement is generally higher than that of Ordinary Portland Cement (OPC) with the same water to binder ratio. Moreover, with the addition of slag, the Ca/Si ratio of C - S - H gel phase usually decrease to near 1.0 [13,14], which can be easily carbonated and transform into an unstable silica gel with a lower molar volume. The increased porosity on the other hand promotes the further diffusion of CO_2, resulting in an enhanced carbonation risk.

Carbonation of cement-based systems is governed by the diffusion of gaseous CO_2 through pores in the matrix, being a time-consuming process [8,12]. Because of this, in laboratory environments, this process is often expedited by increasing the concentration of CO_2, which allows a faster examination of the carbonation effects on cementitious materials. While accelerated carbonation in the lab speeds up the process, it doesn't always reflect natural carbonation accurately. Pastes carbonated with CO_2 concentrations over 3 % show notable differences in mineral composition and microstructure compared to those carbonated naturally [15].

The distinction between natural and accelerated carbonation is particularly noticeable in cement-slag systems, as the unique coloration of slag makes these differences more apparent. It is well known that slag-containing blends, including cement-slag and alkali-activated slag

* Corresponding author at: Stevinweg 1, 2628 CN Delft, the Netherlands.
E-mail address: s.he-2@tudelft.nl (S. He).

https://doi.org/10.1016/j.cemconres.2025.107986
Received 1 January 2025; Received in revised form 1 July 2025; Accepted 6 July 2025
Available online 9 July 2025

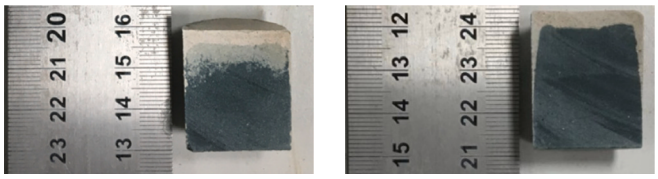

(a) (b)

Fig. 1. (a) Zonation phenomenon observed inside a slag cement paste exposed to air for about two years; (b) another paste with the same mixture carbonated acceleratingly (3 vol%) for 6 months. Only the top sides of both specimens were exposed and the other sides were sealed.

mixtures, both exhibit a blue-green coloration because of the formation of di- and tri-sulfur radical anions under anoxic conditions [16]. The coloration was observed to correlated with concentrations of slag, wherein the color shifted to green and blue with the increase of slag content [17]. When exposed to oxygen (atmosphere), di- and tri-sulfur radical anions is oxidized into $S_2O_3^{2-}$ (intermediate) and SO_4^{2-} (stable) ions [18–20], and the blue-green coloration disappears gradually. When considering the accompanied diffusion of O_2 and CO_2 in slag-containing systems, a zonation phenomenon (areas presenting different intensities in green coloration, *i.e.*, colorless, light green, and blue-green) can be observed inside specimen, as Fig. 1 (a) shows. Owing to the molar mass difference, the diffusion coefficient of oxygen (D_{O2}) is greater than carbon dioxide (D_{CO2}) [21,22]. After a sufficient natural exposure, the different diffusion depths of O_2 and CO_2 led to the formation of zonation displayed in (a). However, this phenomenon was seldom noted in systems under accelerated carbonation (Fig. 1 (b)), where an enhanced CO_2 concentration was employed. It can be explained by the enhanced CO_2 diffusion rate owing to the modification of microstructure under accelerated test [23].

Consequently, this leads to questions about the properties of this transitional zone in slag-containing mixtures under natural carbonation. Theoretically, the carbonated zone undergoes a volume change due to specific factors (*e.g.*, the shrinkage of C - S - H gel phase), while the uncarbonated zone remains stable in volume. This disparity in volume change can cause strain in the transitional zone, potentially altering its microstructure and heightening the risk of cracking. Key inquiries thus include whether this zone places a weak link in transferring load, and how its microstructure, micromechanical, and mineralogical properties differ from other regions. Additionally, comprehending the zonation phenomenon aids in exploring correlations with the diffusion of O_2 (related to corrosion) and CO_2 (pertinent to both corrosion and carbonation) in cement-based systems.

Therefore, in the present investigation, slag-rich cement pastes were prepared and were subjected to natural exposure for an extended carbonation period of two years. The changes on microstructural, micromechanical, and mineralogical properties across different areas were investigated by a set of characterization techniques including mercury intrusion porosimetry (MIP), scanning electron microscope and energy-dispersive x-ray spectroscopy (SEM/EDS), nanoindentation, thermogravimetric analysis (TGA) and quantitative x-ray diffraction (QXRD) analysis. Emphasis was laid on the transitional area extending from the carbonated area. The results obtained in this paper provide insight into the properties of the transitional zone and the zonation phenomenon observed in slag-rich cement paste.

2. Materials and methodology

2.1. Materials

CEM I 42,5 N (NEN-EN 15167-1) from ENCI Maastricht B.V. and slag product provided by Ecocem Benelux B.V. were utilized to produce custom blended slag cement system. Chemical compositions of the cement and slag as determined by X-ray fluorescence spectrometer (XRF) are given in Table 1. The detailed particle size distribution of cement and slag was measured by laser diffraction and is shown in Fig. 2.

Fig. 3 illustrates the spectra of X-ray diffraction (XRD) for slag. As can be seen, it was entirely amorphous as no characteristic peaks can be detected in the diffractogram. Additionally, the amorphous hump was

Table 1
Chemical compositions (wt%) and physical properties of CEM I 42,5 N and slag.

	Cement	Slag
CaO	64.5	41.67
SiO_2	20.4	38.68
Al_2O_3	5.3	9.65
MgO	1.7	7.02
Fe_2O_3	3.2	0.25
TiO_2	–	0.63
MnO	–	0.12
Na_2O	0.5	0.16
K_2O	0.8	0.33
SO_3	2.8	1.23
Others	0.4	0.26
d_{50} (μm)[a]	26.81	31.13

[a] The particle size distribution of cement and slag was measured by EyeTech, Ankersmid.

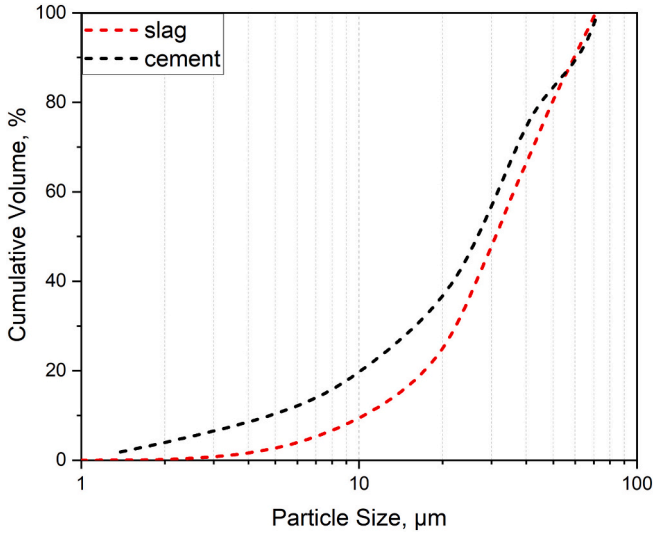

Fig. 2. Particle size distribution of slag.

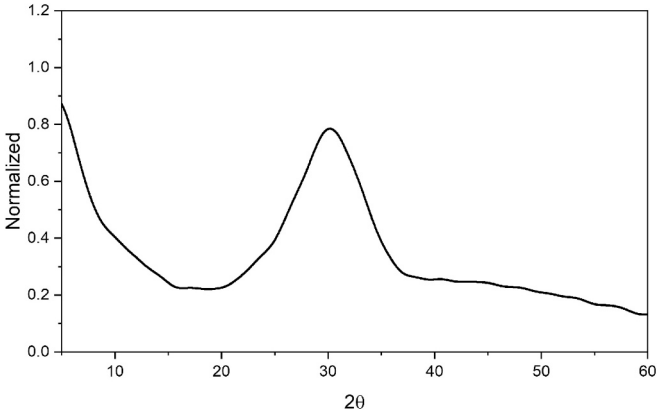

Fig. 3. XRD scan of slag employed in this study.

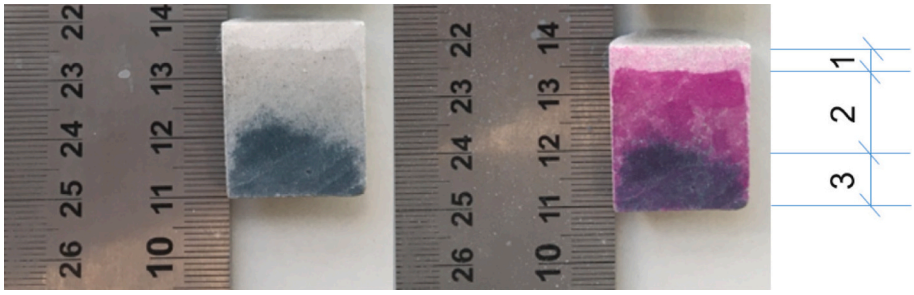

(a)

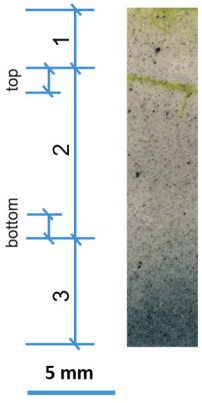

(b)

Fig. 4. (a) Typical sawn surface of slag paste exposed in the laboratory for ~2 years and the coloration change after spraying with phenolphthalein solution, and the division of carbonated (1), transitional (2), and uncarbonated (3) zones; (b) the rough positions of zone 2_top and zone 2_bottom based on digital light microscope (VHX-7000 SERIES).

fluctuated at around 30° (2θ).

2.2. Sample preparation

For the specimens tested in the current study, cement was partially replaced by slag at a constant substitution level of 70 wt%. The replacement ratio was determined such that the composition of specimens was comparable to CEM III/B (NEN-EN 15167-1). The water to binder (cement + slag) ratio was kept at 0.40.

After 3 months of sealed curing, specimens were taken out of the plastic bottles. To avoid being influenced by bleeding, the top layer of the specimen (*i.e.*, around 5 mm in thickness) was sawn off, and only this side was exposed to the environment of laboratory for 2 years. The other sides were sealed to ensure one-dimensional diffusion. The temperature and relative humidity were maintained at 20 ± 5 °C and 50 ± 5 % in the lab, respectively.

2.3. Tests

To prepare samples for analysis at different depths from exposure surface, the specimens were first sliced based on phenolphthalein spray results (*e.g.*, Fig. 4). Then, these slices were immersed in the isopropanol solution for hydration stop, dried at a 40 °C oven, ground to fine powders, and vacuumed for further analysis.

Thermogravimetric analysis (TGA) and Quantitative XRD (Q-XRD) were carried out on ground powders to identify the phase assemblage. Q-XRD data was collected using a Bruker D8 Advance diffractometer Bragg-Brentano geometry and Lynxeye position sensitive detector with Cu K-alpha radiation (using 10 wt% pure silicon as internal standard). The machine was operated with an X-ray beam current of 40 mA at an acceleration voltage of 45 kV. Approximately 1 g of powder was deposited in PMMA sample holder L25 for each mixture. Sample powder was scanned from 5 to 60° (2θ) with a step size of 0.03° and a counting time of 2 s per step. TGA was performed on a Netzsch STA 449 F3 Jupiter coupled with mass spectrometer (MS) Netzsch QMS 430C under Argon atmosphere. The emissions of H_2O and CO_2 from the sample after heating were thus identified. For each test, about 50 mg of sample powder was heated from 40 to 900 °C at a heating rate of 10 °C/min in an Al_2O_3 crucible. The area under the MS CO_2 curve was calculated through a commercial software Origin Pro 2019 (peak integral). This value served as an index to characterize the CO_2 binding degree of different phases in the investigated samples.

Mercury intrusion porosimetry (MIP) analysis was implemented on small crushed particles to measure the properties of pore structure. The relationship between pore diameter (D) and pore pressure (P) is given in Washburn equation [24]:

$$P = -\frac{4\gamma cos(\theta)}{D}$$

of which the surface tension of mercury (γ) is 0.485 N/m at 25 °C and the contact angle between mercury and specimen (θ) is 140°.

In addition, polished sections were also prepared for the microanalysis. During this test, samples were prepared without slicing. They were immersed in isopropanol solution to stop hydration, dried at a 40 °C oven, and impregnated with epoxy resin. Subsequently, sample surfaces were ground and polished down to 1 μm. Finally, these well-polished surfaces were carbon coated at a thickness of about 10 nm. For the microanalysis, a FEI QUANTA FEG 650 ESEM equipped with an Energy Dispersive Spectroscopy (EDS) detector was employed in high vacuum chamber condition. All microanalysis was examined at a working distance of 10 mm and an accelerating voltage of 10 kV,

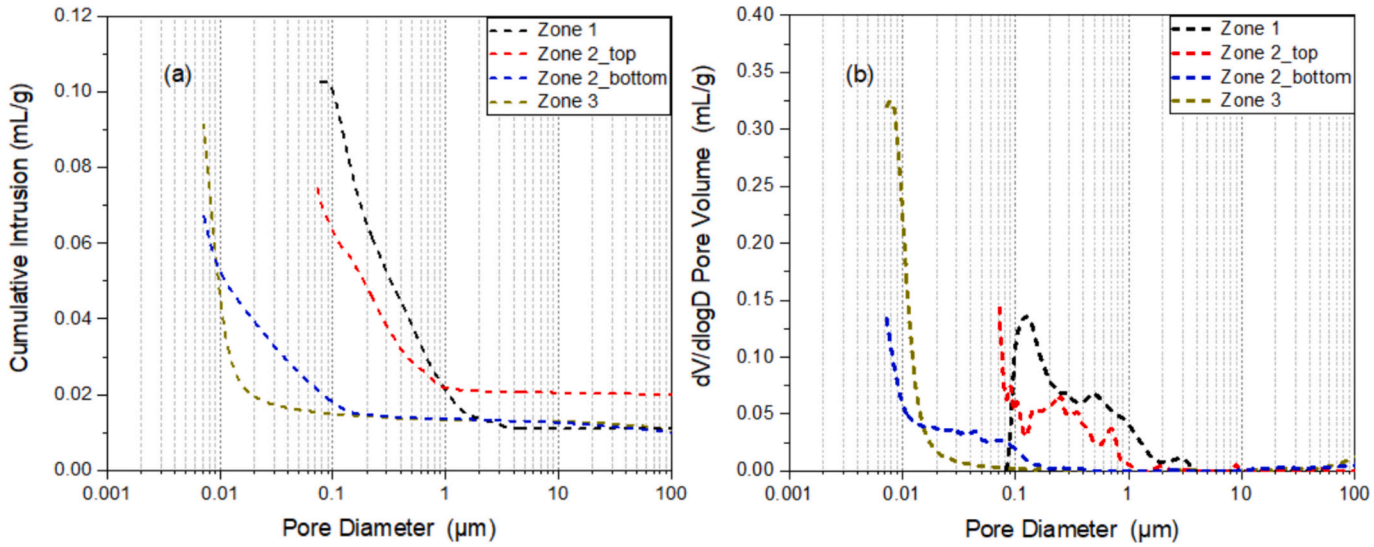

Fig. 5. (a) Cumulative intrusion and (b) differential pore size distribution of carbonated (zone 1), transitional (zone 2_top and zone 2_bottom), and uncarbonated areas (zone 3) of slag paste.

respectively. Phases in cement matrix and slag rims around anhydrate slag particles were characterized by EDS microanalysis with internal standard (standardless microanalysis).

Nanoindentation tests were conducted using a G200 Nanoindenter equipped with a Continuous Stiffness Measurements (CSM) module. Distinct zones, located at varying depths from the exposure surface of slag-rich cement, were selected for analysis. These zones included the carbonated area, the transitional zone near the carbonated area, the transitional zone near the uncarbonated area, and the uncarbonated zone. In each of these designated locations, a grid of 20 × 20 indentations, spaced 20 μm apart, was systematically performed, covering an area of 400 μm × 400 μm. Each indentation was made to a depth of

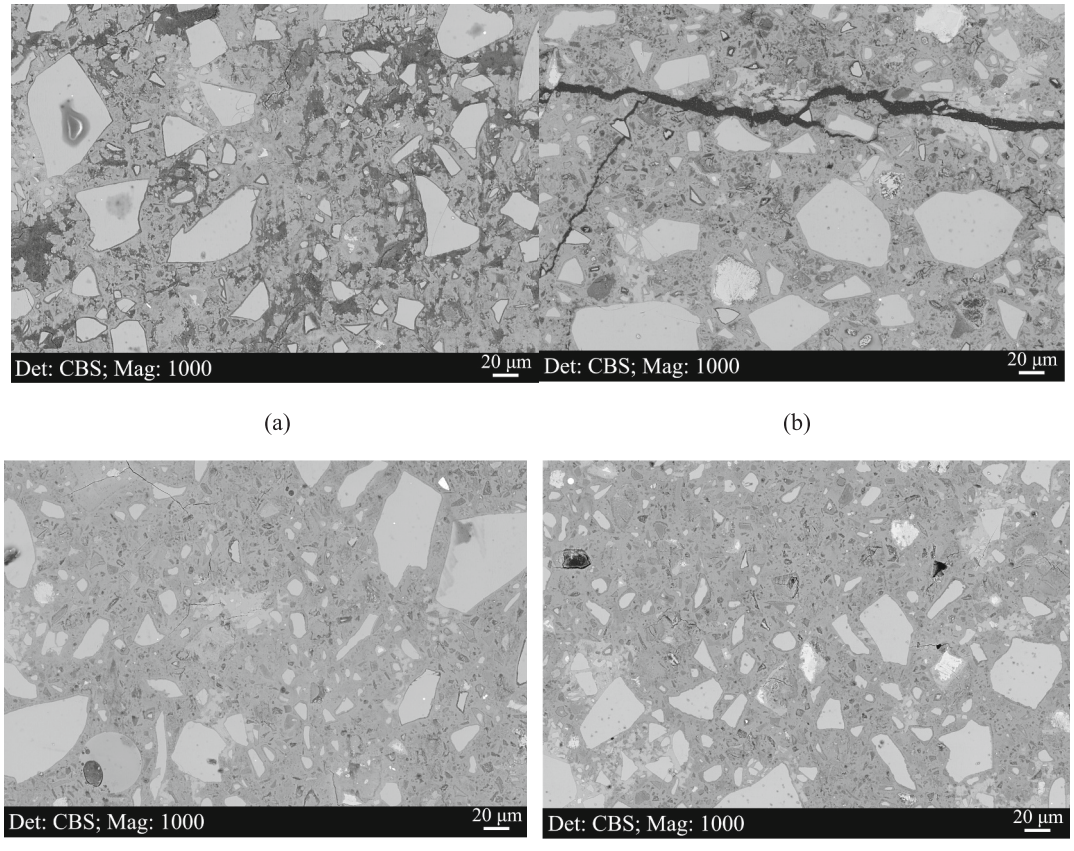

Fig. 6. Typical microstructures of (a) carbonated (zone 1); (b) transitional (zone 2_top); (c) transitional (zone 2_bottom); and (d) uncarbonated areas of slag paste (zone 3).

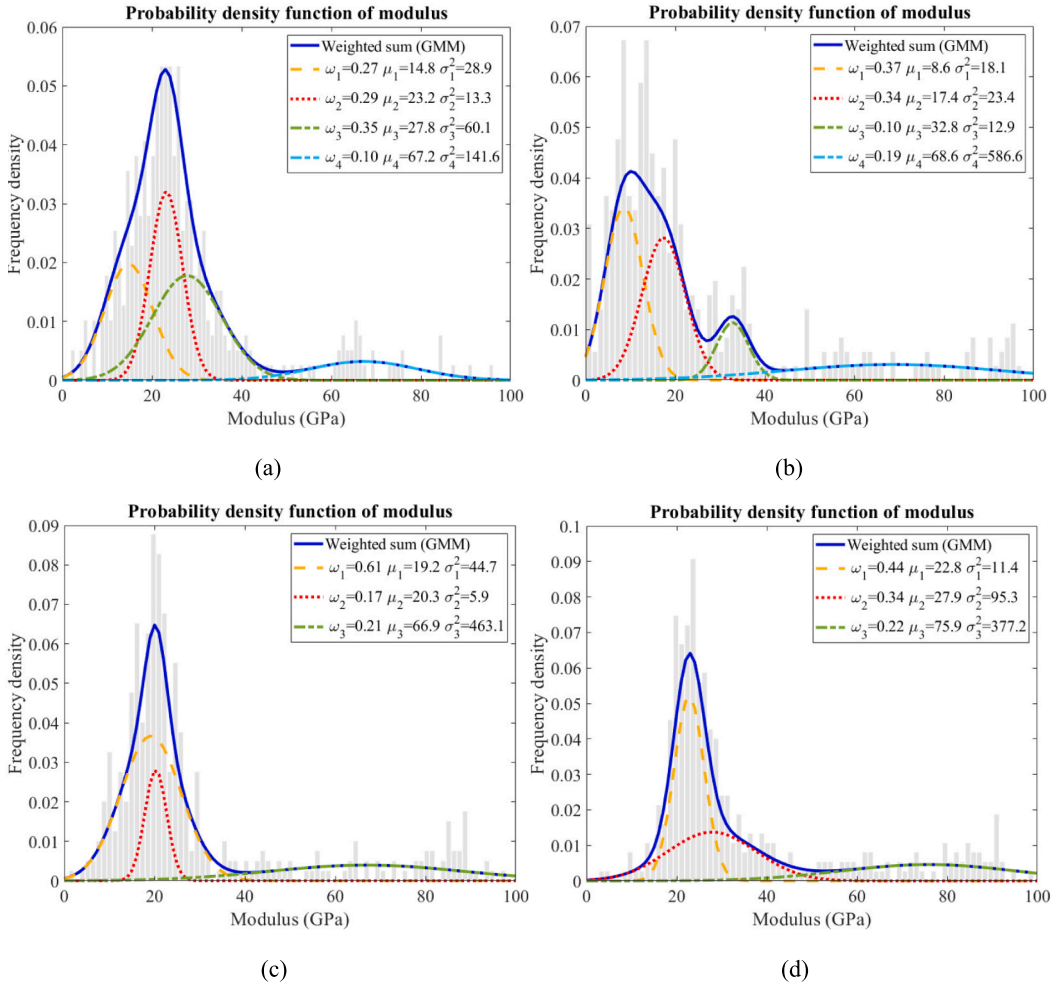

Fig. 7. Indentation modulus of (a) to (d): zone 1, zone 2_top, zone 2_bottom, and zone 3, respectively (ω: weight percentage; μ: mean value; σ: standard deviation).

1000 nm at a consistent strain rate of 0.05 s^{-1}. The CSM module operated at a harmonic frequency of 45 Hz and a displacement of 2 nm. The results for modulus and hardness were determined from the CSM indentation curves by averaging the values obtained between indentation depths of 200 nm and 1000 nm.

3. Results and discussion

3.1. Phenolphthalein spray

The phenolphthalein indicator (1 g phenolphthalein in 100 g mixture of 70 % ethanol and 30 % water) was applied to the freshly broken surface (in 1 min after slicing), and color change was observed once the color had stabilized (1 h after spraying). The typical cross-sectional surface of paste specimen before and after phenolphthalein spray are shown in Fig. 4 (a). As can be seen, zones with three different colors can be seen along carbonation direction, which can be attributed to the different diffusion rate of O_2 and CO_2, leading to varying depth of oxidation and carbonation. The blue-green coloration of zone 3 is known to be originated from the formation of blue-green metal sulfides under anoxic conditions [16,17,25]. Hence, the persistence of this color implies that minimal O_2 has permeated this area, in contrast to zones 1 and 2, which have undergone oxidation. Considering that O_2 diffuses more rapidly than CO_2 within concrete, the green color further suggests that CO_2 has not yet penetrated zone 3.

Unlike zone 3, zone 1 exhibited a noticeable influence from both O_2 and CO_2, as indicated by the fading of its green color and the subsequent shift to pink when phenolphthalein was applied. Remarkably, zone 2 displayed a mix of light green and pink colors, signifying that abundant of oxygen (O_2) present in this region while an insufficient amount of CO_2 had reached this zone to significantly alter the local pH. Given the primary focus of this study on the impact of carbonation, we have classified the three zones as follows: “carbonated zone” (labeled as 1), “transitional zone” (labeled as 2), and “uncarbonated zone” (labeled as 3).

As observed, the carbonation depth extended to approximately 3–4 mm, and the transitional zone reached a depth of nearly 15 mm. Within the substantial transitional zone, we further subdivided it into two distinct sub-zones, each approximately 2 mm in length. These sub-zones are designated as “zone 2_top” located adjacent to the carbonated area, and “zone 2_bottom” positioned along the border of the uncarbonated region. To conduct a thorough analysis, samples were extracted from four specific areas: zone 1 (carbonated), zone 2_top, zone 2_bottom (both transitional), and zone 3 (uncarbonated).

3.2. Microstructure

3.2.1. MIP

Pore size distributions of the four regions tested by Mercury Intrusion Porosimetry are displayed in Fig. 5. Compared with non-carbonated area (zone 3), the critical pore diameter of carbonated area (zone 1) shifted right to the range of 0.1–10 μm with a bimodal mode (Fig. 5 (b)) and an increased total porosity (Fig. 5 (a)). It implied that a coarser pore structure was created after carbonation. This effect can be assigned to the carbonation-induced decalcification of C - S - H gel phase [9,26–29].

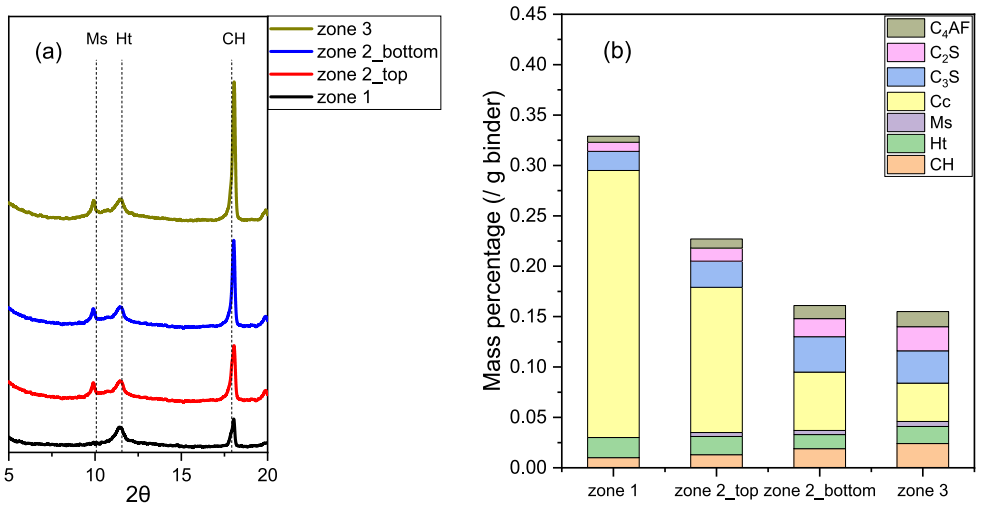

Fig. 8. (a) XRD scans of carbonated (zone 1), transitional (zone 2_top and zone 2_bottom), and uncarbonated areas (zone 3) of slag paste. (b) quantified phase assemblages of four areas. CH: portlandite; Ht: hydrotalcite-like phase; Ms.: calcium monosulfoaluminate; Cc: calcium carbonate.

Notably, the pore structures of the transitional area, especially close to the carbonated zones (zone 2_top), mirrored that of the carbonated area. This similarity indicates that the transitional zone was also substantially affected by carbonation. Although this region exhibited a pink coloration after phenolphthalein spray (Fig. 4), CO_2 had actually entered this area and reacted with C - S - H gel phase, leading to an increased critical pore diameter, in the range of 0.1–1 μm. Conversely, zone 2_bottom remained unaffected by the attack of carbon dioxide, exhibiting a pore structure similar to that of zone 3. This observation further validates our use of the green coloration as a reliable boundary marker to define the end of the transitional zone.

3.2.2. SEM

Figs. 6 show the typical microstructure at different depths. The matrix in the carbonated area (zone 1) underwent considerable degradation, as evidenced by the presence of many dark spots (Fig. 6 (a)). This suggests the creation of extra capillary pores resulting from the decalcification of the C - S - H gel phase, which were later filled with epoxy resin during epoxy impregnation. In zone 2_top, although the number of black spots reduced, interconnected micro-cracks were developed near the boundary with carbonated area (Fig. 6 (b)), possibly due to the differential volume changes of adjacent areas. In the bottom part of transitional area (zone 2_bottom, Fig. 6 (c)) and non-carbonated area (zone 3, Fig. 6 (d)), the matrix was densely intermixed with unhydrated cement clinkers and slag particles. In summary, the results from both SEM and MIP analyses suggest that the damage resulting from carbonation extends beyond the fully carbonated zone (as indicated by phenolphthalein). Moreover, this damage is primarily localized within the zone where the green color fades due to oxidation (transitional zone).

3.3. Micro-mechanical properties

To explore how the additional porosity influences local mechanical properties, nanoindentation tests were conducted across all four zones, with approximately 400 nanoindentations performed in each zone. Detailed statistical deconvolution process of the nanoindentation results can be found in [30].

Distribution of indentation modulus obtained from different areas are shown in Fig. 7 (a) to (d). As can be seen from Fig. 7 (c) and (d), curves in yellow and red, corresponding to low-density and high-density C - S - H gel phase, peak around similar modulus value with a low variance. For zone 2_bottom, the value for low-density is 19.2 ± 6.7 GPa, close to that of zone 3 (22.8 ± 3.4 GPa). This indicates that the micromechanical properties of zone 2_bottom are nearly identical to those of zone 3, suggesting that minimal CO_2 penetration occurred in zone 2_bottom.

Regarding zone 1 and zone 2_top (as shown in Fig. 7 (a) and (b)), there is a noticeable decrease in the modulus values of the C - S - H gel phases compared to the those of zone 2_bottom and zone 3, which is due to the degradation or decalcification after CO_2 attack. Notably, regarding zone 2_top, the frequency distribution of the low-density C-S-H gel phase (yellow curve) has shifted significantly towards the lower end, concentrating at 8.6 ± 4.3 GPa, which is lower than that of zone 2_bottom (19.2 ± 6.7 GPa) and zone 3 (22.8 ± 3.4 GPa). It is important to note that this value is even lower than that of the fully carbonated zone (zone 1), which is approximately 14.8 GPa. This suggests that CO_2-induced degradation can be more severe in the transitional zone compared to the fully carbonated zone. Even though zone 2 displayed pink coloring post-phenolphthalein spray, implying it was non-carbonated, the micro-mechanical properties of this area close to the carbonated zone had notably reduced. This observation aligns with the results obtained from MIP and SEM analyses (Section 3.2).

3.4. Mineralogical properties (phase assemblage)

To further investigate the carbonation degree of the transitional zone, a comprehensive mineralogical investigation was conducted. Thermal analysis (TG-DTG-MS), quantitative X-ray Diffraction (QXRD), energy-dispersive X-ray spectroscopy (EDS), have been performed to investigate the evolution of phase assemblage across different areas.

3.4.1. QXRD

Fig. 8 (a) shows the XRD spectra of phase assemblage in the carbonated, transitional (top and bottom), and non-carbonated areas (5–20° for highlight). As can be seen, hydrotalcite-like phase was seen in each region, despite that its composition had been altered (carbonated). Monosulfate was not detected in the carbonated area, while it was visible in the transitional and uncarbonated zones [31,32]. The peak intensity of portlandite increased significantly from carbonated to non-carbonated area, suggesting that the carbonation degree reduced with depth.

Fig. 8 (b) reveals the quantified phase assemblages of four areas, using open-source software Profex [33]. It should be noted that the unlabeled part in each stacked column consisted of various amorphous phases, including unhydrated slag grains, C - S - H gel phase, and silica gel phase (carbonation product of C - S - H gel phase), *etc.* It was evident that amorphous phases dominated in all regions, and their contents

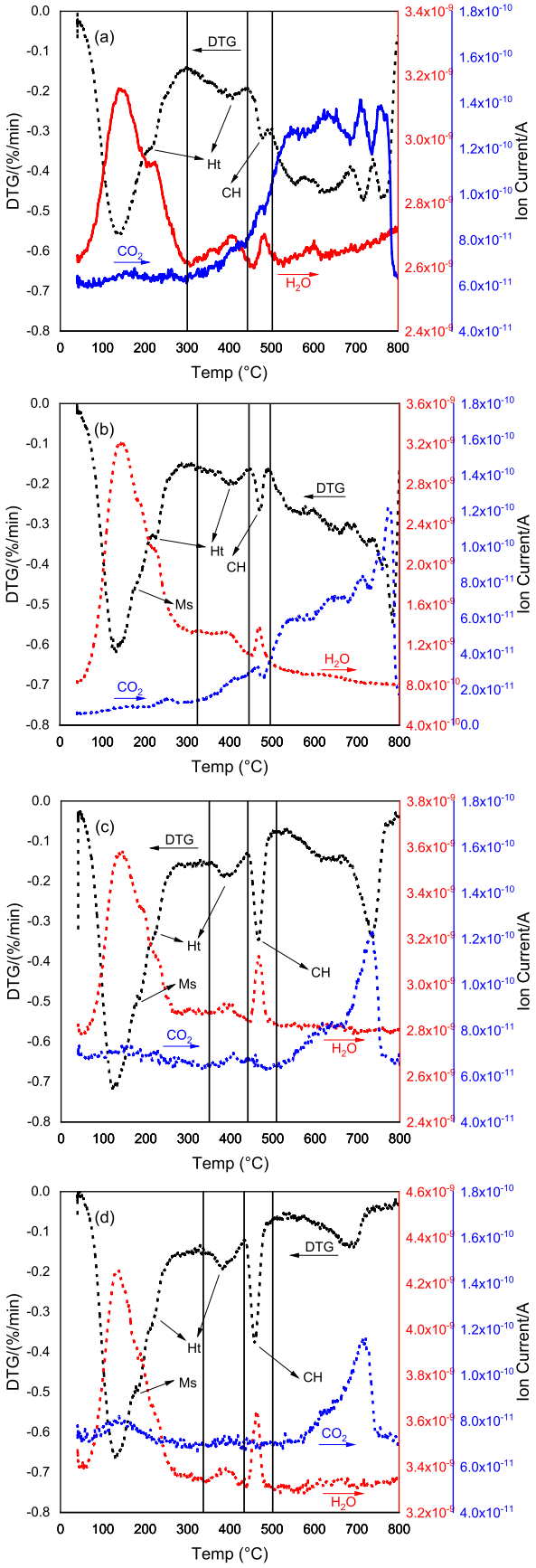

Fig. 9. The DTG results, H_2O and CO_2 MS curves of (a) carbonated (zone 1); (b) transitional (zone 2_top); (c) transitional (zone 2_bottom); and (d) uncarbonated areas of slag paste. CH: portlandite; Ht: hydrotalcite-like phase; Ms.: calcium monosulfoaluminate.

Table 2
The CO_2 concentration (/100 g binder) of carbonated hydrotalcite-like phase and calcium carbonate obtained from QXRD and TG-DTG-MS.

	CO_2 concentration (/100 g binder)			
	Carbonated hydrotalcite-like phase		Calcium carbonate	
	QXRD[a]	TG-DTG-MS	QXRD	TG-DTG-MS
Carbonated	0.18	2.44	11.66	13.32
Transitional_top	0.16	1.15	6.34	7.11
Transitional_bottom	0.13	0.37	2.55	2.52
Uncarbonated	0.15	0.30	1.67	1.98

[a] Note that the CO_2 binding ability of hydrotalcite depends on its Mg/Al ratio. As can be seen in Fig. 11 (b), the Mg/Al ratio carbonated hydrotalcite-like phase was close to (slightly higher than) 4:2, thus $Mg_4Al_2(OH)_{12}(CO_3)\bullet 4(H_2O)$) was assumed as the stoichiometric formula of this phase in the paper.

decreased remarkably in the carbonated zone, due to the carbonation of amorphous C - S - H gel phase and the thus formation of crystalline calcium carbonate. Additionally, note that the amount of hydrotalcite-like phase levelled off roughly, in the range of 1.5–2.0 wt. The portlandite content remained low, even in the uncarbonated area, approximately at 2.5 wt%. This is attributed to the 70 wt% slag replacement level and the age of the specimens, which is 2 years. Also, it was noted that the amounts of unhydrated cement clinkers (C_3S, C_2S, and C_4AF) reduced gradually from non-carbonated to carbonated area, which was related to the direct carbonation of clinker phases [34,35].

Aligning with the findings from thermal analysis presented in Fig. 9, the hydration products in Zone 2_top underwent significant carbonation, contrasting with Zone 2_bottom in terms of carbonation degree. Even though the entire zone 2 displayed pink coloring post-phenolphthalein spray, the calcium carbonate content in Zone 2_top was over twice that of Zone 2_bottom, indicating extensive degradation from CO_2 attack. Taking into account the micromechanical characterization results discussed in Section 3.3, it can be inferred that the phenolphthalein spray might not accurately determine the carbonation depth in slag-rich cement.

Table 2 compares the CO_2 concentration (/100 g binder) of carbonated hydrotalcite-like phase and calcium carbonate obtained from QXRD and TG-DTG-MS. For CO_2 concentration in calcium

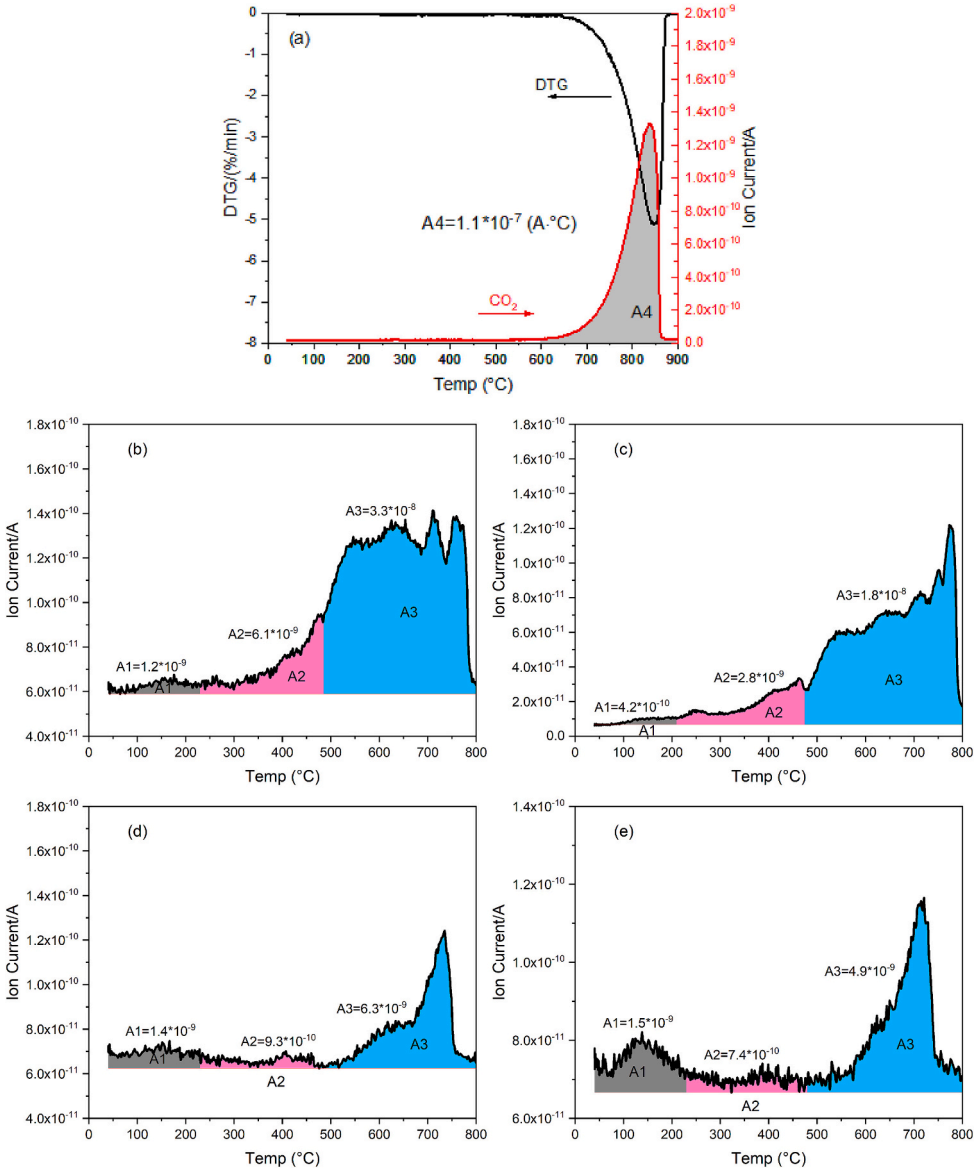

Fig. 10. (a) The DTG result, CO_2 MS curve of pure $CaCO_3$; (b-e) The CO_2 MS curve of slag paste in the carbonated, transitional (top and bottom), and non-carbonated areas, respectively.

Table 3
The calculated areas under MS CO_2 curve and the corresponding CO_2 concentration of each carbonate phase (/100 g binder).

	Area under the MS CO_2 curve (A•°C)			Total
	Carbonated Ca—Al AFm phases	Carbonated hydrotalcite-like phase	Calcium carbonate	
Pure $CaCO_3$	–	–	$1.1 * 10^{-7}$	$1.1 * 10^{-7}$
Carbonated	$1.2 * 10^{-9}$	$6.1 * 10^{-9}$	$3.3 * 10^{-8}$	$4.0 * 10^{-8}$
Transitional_top	$4.2 * 10^{-10}$	$2.8 * 10^{-9}$	$1.8 * 10^{-8}$	$2.1 * 10^{-8}$
Transitional_bottom	$1.4 * 10^{-9}$	$9.3 * 10^{-10}$	$6.3 * 10^{-9}$	$8.6 * 10^{-9}$
Uncarbonated	$1.5 * 10^{-9}$	$7.4 * 10^{-10}$	$4.9 * 10^{-9}$	$7.1 * 10^{-9}$
	CO_2 concentration of each carbonate phase (/100 g binder)			Total
	Carbonated Ca—Al AFm phases	Carbonated hydrotalcite-like phase	Calcium carbonate	
Pure $CaCO_3$	–	–	44.0	44.0
Carbonated	0.5	2.4	13.3	16.2
Transitional_top	0.2	1.1	7.1	8.4
Transitional_bottom	0.6	0.4	2.5	3.5
Uncarbonated	0.6	0.3	2.0	2.9

carbonate, the measured values were similar between these two quantitative techniques. This is because that various polymorph of calcium carbonate, including amorphous calcium carbonate, metastable calcium carbonate (aragonite and vaterite), and calcite were present simultaneously in a carbonated cement-based system [36–38]. Under long term natural exposure, amorphous carbonate was converted into metastable and stable forms gradually through dissolution-precipitation process [38], which thus can be detected by XRD. In contrary, for CO_2 content in carbonated hydrotalcite-like phase, relatively large discrepancy was identified between values obtained from two techniques, and significantly higher values were given by TG-DTG-MS. This is because that XRD can only detect CO_2 which is chemically bound in the crystalline phase, *e.g.*, $Mg_4Al_2(OH)_{12}(CO_3)•4(H_2O)$. However, because of its layered microstructure, hydrotalcite-like phase exhibits a large specific surface area comparable to C - S - H gel phase [39], which provides numbers of natural site to fix free CO_2 molecules both physically and chemically [40,41]. As confirmed in [42,43], physically bound CO_2 molecules started to be released from 250 °C while this portion cannot be measured by XRD. These reasons explained the reduced CO_2 concentration in carbonated hydrotalcite-like phase determined by XRD.

3.4.2. TG-DTG-MS

Figs. 9 (a)-(d) present the DTG (derivative thermogravimetry) results and mass spectrometer (MS) curves of the four regions, respectively. As can be seen from Fig. 9 (a), the specimen experienced a heavy CO_2 attack in the carbonated zone (zone 1). No calcium monosulfoaluminate (monosulfate in short) can be detected in this part, for that no shoulder like plateau can be observed in the curve around 200 °C. Although calcium hydroxide, which decomposes between 450 and 500 °C, was still observed, the amount of it was far less than that of uncarbonated region (zone 3) as shown in Fig. 9 (d). The main CO_2-bearing phases in this area were calcium carbonate, sourcing from the reaction between CO_2 and calcium hydroxide as well as C - S - H gel phase. Hydrotalcite-like phase was also carbonated, verified by the increase in the ion current intensity of CO_2 at ~250 °C and 350–450 °C. The small hump occurring at 100–200 °C of CO_2 MS curve was assigned to the formation of carbonated Ca—Al AFm phases [26,31,32].

Compared to zone 1, zone 2_top in the transitional part experienced a less but also significant CO_2 attack as revealed in Fig. 9 (b). A notable reduction in portlandite content and increase in calcium carbonate formation can be observed. By comparing Fig. 9 (c) and (d), it is observed that both Zone 2_bottom and Zone 3 display similar

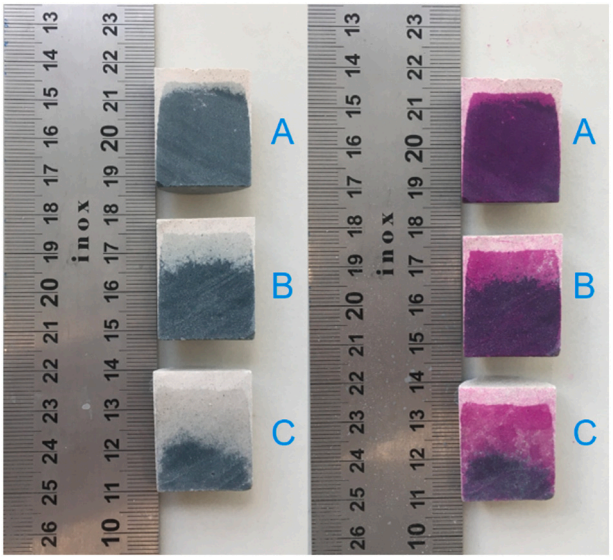

Fig. 12. Three typical sawn surfaces of blended cement paste A, B, and C with different slag chemistries. They were cast in the same batch and exposed in the laboratory for ~2 years. As can be seen, their transitional areas presented significantly variable widths.

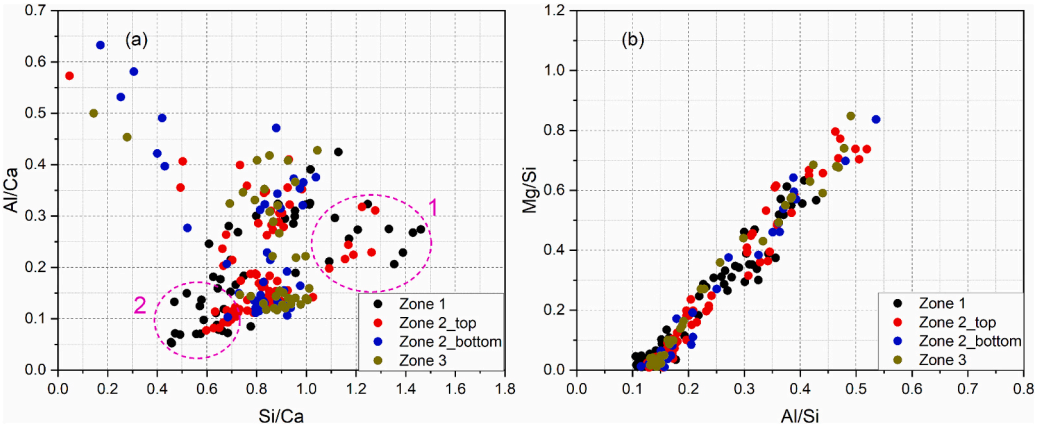

Fig. 11. Typical plots of (a) Al/Ca against Si/Ca and (b) Mg/Si against Al/Si in atomic ratio of slag paste at different depths.

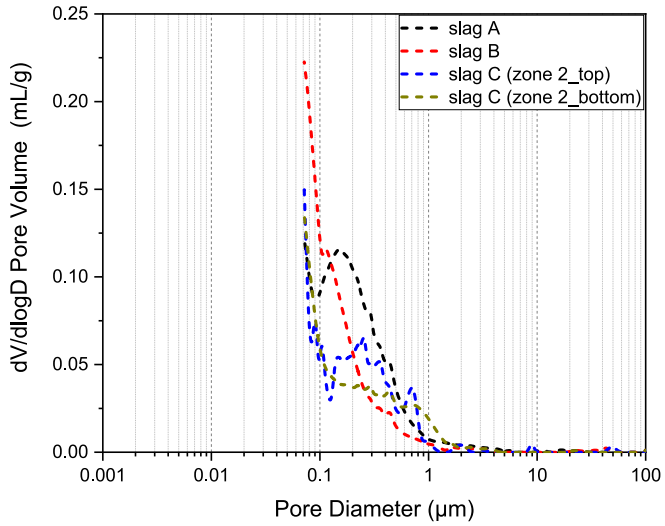

Fig. 13. Differential pore size distribution of transitional area of slag paste A, B, and C (top and bottom).

carbonation characteristics, evidenced by the detection of monosulfate. Additionally, a substantial amount of Ca(OH)2 was found to remain in these zones. Overall, there was a gradual decrease in the amount of CO_2 penetration along the exposed direction. Notably, Zone 2_top and Zone 2_bottom exhibited markedly different degrees of carbonation, with the hydration products in Zone 2_top undergoing significant carbonation. This observation supports our classification of Zone 2 as a critical transition zone, highlighting its unique role in the carbonation process.

To quantify CO_2 content in different CO_2-bearing phases at different depths, high quality $CaCO_3$ (calcite, from VWR Chemicals BDH) was adopted as standard specimen [26,31]. Fig. 10 (a) illustrates the DTG result, CO_2 MS graph of pure $CaCO_3$. The area under the MS CO_2 curve (A•°C) corresponding to 44 wt% CO_2 releasing from $CaCO_3$ was determined using software OriginPro 2019. Similarly, the CO_2 uptake profile across different areas can thus be calculated, which are revealed in Figs. 10 (b)-(e).

Calcium carbonate presents several different polymorphs in the carbonated cementitious materials which decompose from around 500 °C [36–38]. Although their decomposition peaks overlap with each other, it does not affect the determination of total CO_2 bound in calcium carbonate. As for carbonated hydrotalcite-like phase, it releases CO_2 from 250 to 450 °C [42,43]. Fortunately, no other phases releases CO_2 at this range in the carbonated slag cement paste. Therefore, the areas A1, A2, and A3 in Fig. 10 (b)-(e) correspond to the amount of CO_2 released from carbonated Ca—Al AFm phases, carbonated hydrotalcite-like phase, and calcium carbonate, respectively.

The calculated areas under MS CO_2 curve and the corresponding CO_2 concentration of each carbonate phase (/100 g binder) in the sample is given in Table 3. As can be seen, the amount of absorbed CO_2 decreased when moving from carbonated to non-carbonated region. Different polymorphs of calcium carbonate were the primary CO_2-bearing phases, with approximately 80 % of the CO_2 being sequestered in these phases. The remaining CO_2 (approximately 20 %) was jointly absorbed by carbonated Ca—Al AFm phases and, notably, the hydrotalcite-like phase.

Similar to the results in Sections 3.4.1 and 3.4.2, the top and bottom subzones in the transitional part showed different degrees of CO_2 uptake. The CO_2 concentration in calcium carbonate in the zone 2_top was about 2.5 times that of zone 2_bottom. In addition, around threefold CO_2 was fixed by hydrotalcite-like phase in the top of transitional area.

3.4.3. SEM-EDS

The elemental compositions of hydrated phases in cement matrix and rims around unhydrated slag grains in different positions were characterized by SEM-EDS microanalysis with internal standards (standardless microanalysis). Typical plots of Al/Ca against Si/Ca and Mg/Si against Al/Si in atomic ratios are reported in Figs. 11 (a) and (b), respectively. In general, the measured Ca/Si atomic ratios of C - S - H gel phase fluctuated at around 1.0, in good agreement with the values reported in [13,41]. Substantial decalcification occurred in the carbonated and top of transitional zones, and decalcified C - S - H gel phase existed with lower Ca/Si ratio, circle 1 in Fig. 11 (a). As for points in circle 2 with

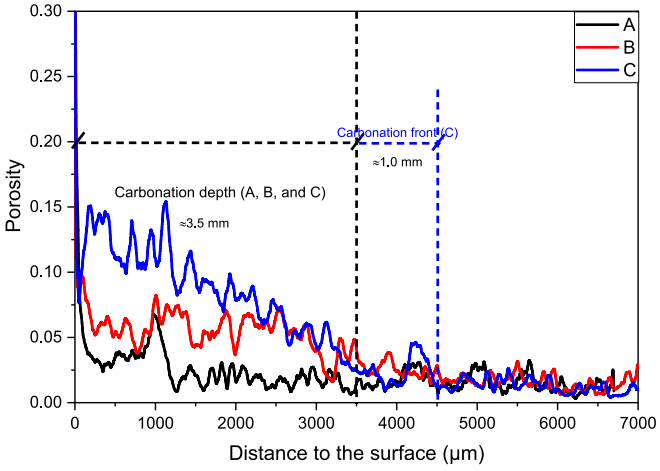

Fig. 15. The 2D-local porosity of slag A, B, and C pastes along carbonation direction. It was measured by thresholding the BSE images (2.47 μm/pixel) at first and subsequently smoothed by the average of adjacent 200 pixels.

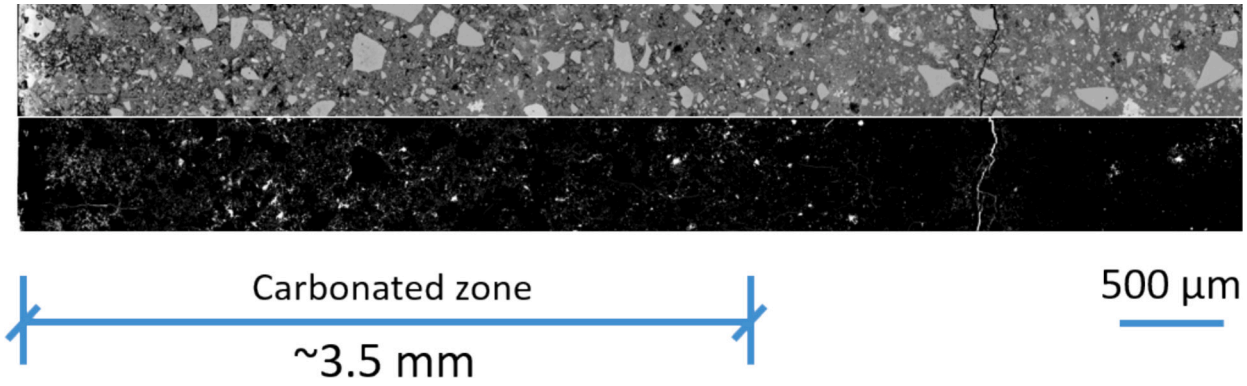

Fig. 14. BSE images of slag paste (a) A, (b) B, and (c) C along carbonation direction. Top: BSE image; and Bottom: BSE image after segmentation for pores (<30 and >30 pixel value).

Table 4
The calculated areas under MS CO_2 curve of each carbonate phase in the carbonated and transitional areas (/100 g binder).

		Area under the MS CO_2 curve (A•°C)			Total
		Carbonated Ca—Al AFm phases	Carbonated hydrotalcite-like phase	Calcium carbonate	
Transitional	Sample A	$0.8 * 10^{-9}$	$0.9 * 10^{-9}$	$5.1 * 10^{-9}$	$6.8 * 10^{-9}$
	Sample B	$1.1 * 10^{-9}$	$1.1 * 10^{-9}$	$6.6 * 10^{-9}$	$8.8 * 10^{-9}$
	Sample C (zone 2_top)	$4.2 * 10^{-10}$	$2.8 * 10^{-9}$	$1.8 * 10^{-8}$	$2.1 * 10^{-8}$
	Sample C (zone 2_bottom)	$1.4 * 10^{-9}$	$9.3 * 10^{-10}$	$6.3 * 10^{-9}$	$8.6 * 10^{-9}$
Carbonated	Sample A	$1.5 * 10^{-9}$	$1.1 * 10^{-8}$	$3.8 * 10^{-8}$	$5.0 * 10^{-8}$
	Sample B	$1.2 * 10^{-9}$	$6.9 * 10^{-9}$	$3.7 * 10^{-8}$	$4.5 * 10^{-8}$
	Sample C	$1.2 * 10^{-9}$	$6.1 * 10^{-9}$	$3.3 * 10^{-8}$	$4.0 * 10^{-8}$

extremely low Si/Ca ratio, some calcium carbonate had probably been incorporated into measurements.

The hydrotalcite-like phase formed in slag rims seemed to be unaffected by CO_2 attack. The Mg/Al atomic ratio derived from the regression analysis of Mg/Si *vs.* Al/Si scatter plot (Fig. 11 (b)) remained nearly the same in each zone. It also indicated that this phase kept intact during carbonation, *i.e.*, the CO_2 uptake in the interlayer space would not decompose the network structure of hydrotalcite-like phase [26,31].

3.5. Transitional area of different widths

To further investigate the features of the transitional zone, several blended cement pastes with different slag chemistries were investigated. Three representative examples were illustrated in Fig. 12. The sample examined earlier is sample "C", which has the most obvious transitional zone. Although they exhibited a similar carbonation depth in 3–4 mm, the width of transitional area varied considerably among them. Some characterization presented above were repeated to determine if the conclusions are applicable to slag with different composition.

Fig. 13 displays the differential pore size distribution of transitional area of each paste. Note that zone 2_top of slag paste C gave the largest critical pore diameter in this region, *i.e.*, several hundred nanometers. Considering the mean free path of 73 nm for O_2 [21] which was notably smaller than the critical pore diameter, normal diffusion was expected to dominate in the pore structure of zone 2_top of slag paste C. As for slag paste A, no distinct peak can be seen in the range of 0.1–1.0 μm. In other words, gel pores and small capillary pores, with a diameter <100 nm, dominated here. Therefore, the mean free path of O_2 roughly equaled to, or was larger than pore diameter slightly. Under this circumstance, Knudsen diffusion prevailed in the transitional area of slag paste A, which was substantially slower than normal diffusion occurring in larger pores in slag paste C [21,22], leading to a reduced width of transitional area observed in slag paste A.

Furthermore, polished section of paste C was utilized as an example to obtain back-scattered electron (BSE) images (Fig. 14) for porosity characterization. The segmentation of pores was carried out on BSE images by thresholding grey pixel value (< 30) [44]. Besides, Fig. 15 presents the 2D-local porosity of slag A, B, and C pastes along carbonation direction, according to the segmentation results of a 2 mm (perpendicular to carbonation direction) × 7 mm (parallel to carbonation direction) area.

Slag paste A presented the smallest porosity in the carbonated area, and the local porosity levelled off at roughly 2.5 % when moving into the transitional zone. Comparatively, slag paste C was more porous after carbonation, although it displayed a similar carbonation depth to the others. Its local porosity decreased gradually when approaching the boundary with transitional region. Unlike slag paste A and B, the porosity of slag paste C fluctuated dramatically when entering the transitional area. The local porosity reduced to close 2.5 % after additional ~1.0 mm. Moreover, continuous micro-cracks were propagated into this region (Fig. 14). As explained in [45–47], this area was also named as 'dissolution area', and it was a reactive part where Ca-bearing phases (including portlandite and C - S - H gel phase) progressively decalcified, and the porosity was thus increased here.

The variation in the widths of the transitional areas observed in slag pastes A, B, and C is thought to be associated with the distinct CO_2 binding capacities of each mixture. Table 4 gives the calculated areas under MS CO_2 curve of each carbonate phase in the carbonated and transitional areas of them. As can be seen, slag paste A bound the most CO_2 in the carbonated area per 100 g binder while the least for slag paste C. In other words, slag paste A showed a stronger CO_2 binding capacity and a higher degree of carbonation.

As less CO_2 was bound in the carbonated zone, more CO_2 entered the transitional region of slag paste C. These diffused CO_2 induced the partial carbonation of cement matrix in this area and modified the microstructure, as a result. Especially for the part close to the boundary with carbonated zone, black spots indicating the formation of capillary pores were frequently detected (Fig. 6 (b)). Continuous micro-cracks

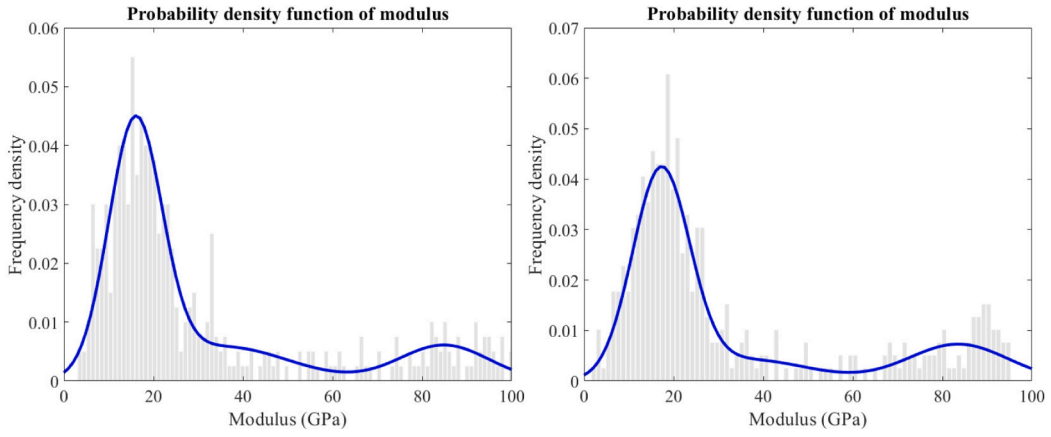

(a) (b)

Fig. 16. Indentation modulus of transitional area of (a) slag B and (b) slag C pastes, respectively.

also penetrated into this part (Fig. 6 (b) and Fig. 14). The enlarged porosity in turn promoted the diffusion of O_2, leading to a wider transitional zone seen in slag paste C.

The relative frequency of indentation modulus obtained from the transitional area of slag paste A and B are shown in Fig. 16 (a) and (b), respectively. The highest peak in the frequency histogram of both graphs was supposed to be C - S - H gel phase. Interestingly, no obvious degradation regarding the micro-mechanical properties of C - S - H gel phase (~19.0 GPa) was detected for these two samples in the transitional region.

In fact, the essence of transitional area occurring in slag-containing systems under natural carbonation can be explained by the concept 'carbonation front' [37,44,48]. This term is defined as the zone sandwiched between carbonated and non-carbonated areas. Its width can be determined through XRD, thermogravimetry, Raman spectroscopy, pore solution, *etc.* [36,38,49,50]. The work in [37] demonstrated that the width of carbonation front was directly linked to the ratio of two time scales, τ_R and τ_D, which were associated with the carbonation reaction rate and CO_2 diffusion coefficient, respectively. It was calculated that the more porous the microstructure was, the broader the carbonation front was. These conclusions were in good agreement with results obtained in the current study. According to the 2D-local porosity profile determined in Fig. 15, slag paste A exhibited the smallest porosity in the carbonated region. Correspondingly, it illustrated a negligible transitional region as observed in Fig. 12. As for slag paste B and C, the carbonation front was smooth as the 2D-local porosity reduced gradually when moving from carbonated to transitional zone. Correspondingly, the width of transitional area increased for these two pastes.

Therefore, besides carbonation depth commonly measured by phenolphthalein spray, the width of transitional area (visual inspection) can be adopted as another indicator to assess the carbonation resistance of slag-containing systems, especially for mixtures presenting similar carbonation depths. It can be concluded that the wider the transitional area, the smoother the carbonation front, the more porous the microstructure of carbonated and transitional areas. Emphasis should also be laid on the part near the boundary with carbonated zone, where the porosity increased compared to the other parts of transitional zone. It provided more transport passages for the upcoming O_2 and CO_2, thus weakening the carbonation resistance and enhancing the corrosion risk of reinforcement in concrete structures.

4. Conclusions

The paper investigated the changes on microstructural, micromechanical, and mineralogical properties across different areas of slag-rich cement paste after long-term indoor exposure. Emphasis was mainly laid on the transitional zone. The main conclusions drawn were as follows:

1. Carbonation-induced damage extends beyond the fully carbonated zone identified by phenolphthalein. Particularly in the transitional area adjacent to the carbonated zone, which appears pink after phenolphthalein application, there is clear evidence of microstructural damage caused by carbonation as verified by MIP and SEM.
2. Nanoindentation findings confirm that the micromechanical properties of the transitional zones are inferior to those of the uncarbonated zone. Notably, the section of the transitional zone near the carbonated area is especially fragile, showing weaker properties than even the fully carbonated zone, likely a result of microcrack formation in this region.
3. Mineralogical analysis indicates that the transitional zone underwent carbonation, even though it turned pink post-phenolphthalein application. The depth of carbonation stays within the range where slag-containing blends loss its green coloration, which validates the use of the green coloration as a reliable boundary marker to define the transitional zone.
4. The width of the transitional area can serve as an indicator for evaluating the carbonation resistance of slag-containing blends and potentially the corrosion potential. A wider transitional area indicates a smoother carbonation front.

CRediT authorship contribution statement

Yu Zhang: Writing – original draft, Visualization, Project administration, Methodology, Investigation, Formal analysis, Data curation, Conceptualization. **Shan He:** Writing – review & editing, Writing – original draft, Methodology, Investigation, Formal analysis. **Xuhui Liang:** Investigation, Formal analysis, Data curation. **Minfei Liang:** Writing – review & editing, Formal analysis, Data curation. **Oğuzhan Çopuroğlu:** Writing – review & editing, Supervision, Project administration, Funding acquisition. **Erik Schlangen:** Writing – review & editing, Supervision, Project administration, Funding acquisition.

Declaration of competing interest

The authors declare that they have no known competing financial interests or personal relationships that could have appeared to influence the work reported in this paper.

Acknowledgements

Fundamental Research Funds for the Central University (Grant Number RF1028623287) is gratefully acknowledged for the financial support. Authors thank Arjan Thijssen (Microlab, TU Delft) for his technical support. René Albers (Ecocem Benelux B.V.) is gratefully acknowledged for providing commercial slags. Shan He acknowledges the financial supports from the MSCA-ITN project SMARTINCS. This project has received funding from the European Union's Horizon 2020 research and innovation programme under the Marie Skłodowska-Curie grant agreement No 860006.

Data availability

Data will be made available on request.

References

[1] Y. Yang, K. Raipala, L. Holappa, Ironmaking, in: Treatise on Process Metallurgy, Elsevier, 2014.
[2] E. Aprianti, A huge number of artificial waste material can be supplementary cementitious material (SCM) for concrete production–a review part II, J. Clean. Prod. 142 (2017) 4178–4194.
[3] M.C. Juenger, R. Snellings, S.A. Bernal, Supplementary cementitious materials: new sources, characterization, and performance insights, Cem. Concr. Res. 122 (2019) 257–273.
[4] G. Osborne, Durability of Portland blast-furnace slag cement concrete, Cem. Concr. Compos. 21 (1) (1999) 11–21.
[5] B.S. Divsholi, T.Y.D. Lim, S. Teng, Durability properties and microstructure of ground granulated blast furnace slag cement concrete, Int. J. Concr. Struct. Mater. 8 (2) (2014) 157–164.
[6] A.M. Rashad, An overview on rheology, mechanical properties and durability of high-volume slag used as a cement replacement in paste, mortar and concrete, Constr. Build. Mater. 187 (2018) 89–117.
[7] V.G. Papadakis, Effect of supplementary cementing materials on concrete resistance against carbonation and chloride ingress, Cem. Concr. Res. 30 (2) (2000) 291–299.
[8] S. Greve-Dierfeld, B. Lothenbach, A. Vollpracht, et al., Understanding the carbonation of concrete with supplementary cementitious materials: a critical review by RILEM TC 281-CCC, Mater. Struct. 53 (6) (2020) 1–34.
[9] B. Wu, G. Ye, Development of porosity of cement paste blended with supplementary cementitious materials after carbonation, Constr. Build. Mater. 145 (2017) 52–61.
[10] H. Justnes, J. Skocek, T.A. Østnor, et al., Microstructural changes of hydrated cement blended with fly ash upon carbonation, Cem. Concr. Res. 137 (2020) 106192.
[11] V.G. Papadakis, C.G. Vayenas, M. Fardis, A reaction engineering approach to the problem of concrete carbonation, AICHE J. 35 (10) (1989) 1639–1650.
[12] B. Šavija, M. Luković, Carbonation of cement paste: understanding, challenges, and opportunities, Constr. Build. Mater. 117 (2016) 285–301.

[13] R. Taylor, I. Richardson, R. Brydson, Composition and microstructure of 20-year-old ordinary Portland cement–ground granulated blast-furnace slag blends containing 0 to 100% slag, Cem. Concr. Res. 40 (7) (2010) 971–983.
[14] B. Kolani, L. Buffo-Lacarrière, A. Sellier, et al., Hydration of slag-blended cements, Cem. Concr. Compos. 34 (9) (2012) 1009–1018.
[15] M. Auroy, S. Poyet, P. Le Bescop, et al., Comparison between natural and accelerated carbonation (3% CO_2): impact on mineralogy, microstructure, water retention and cracking, Cem. Concr. Res. 109 (2018) 64–80.
[16] J. Couvidat, C. Diliberto, E. Meux, et al., Greening effect of concrete containing granulated blast-furnace slag composite cement: is there an environmental impact? Cem. Concr. Compos. 113 (2020) 103711.
[17] M. Chaouche, X. Gao, M. Cyr, et al., On the origin of the blue/green color of blast-furnace slag-basedmaterials: sulfur K-edge XANES investigation, J. Am. Ceram. Soc. 100 (2017) 1707–1716.
[18] D. Le Cornec, Q. Wang, L. Galoisy, et al., Greening effect in slag cement materials, Cem. Concr. Compos. 84 (2017) 93–98.
[19] A.P. Schwab, J. Hickey, J. Hunter, et al., Characteristics of blast furnace slag leachate produced under reduced and oxidized conditions, J. Environ. Sci. Health A 41 (3) (2006) 381–395.
[20] B. Lothenbach, G. Le Saout, M. Ben Haha, et al., Hydration of a low-alkali CEM III/B–SiO_2 cement (LAC), Cem. Concr. Res. 42 (2) (2012) 410–423.
[21] Y.F. Houst, F.H. Wittmann, Influence of porosity and water content on the diffusivity of CO_2 and O_2 through hydrated cement paste, Cem. Concr. Res. 24 (6) (1994) 1165–1176.
[22] A. Leemann, R. Loser, B. Münch, et al., Steady-state O_2 and CO_2 diffusion in carbonated mortars produced with blended cements, Mater. Struct. 50 (6) (2017) 1–7.
[23] V. Dutzer, W. Dridi, S. Poyet, et al., The link between gas diffusion and carbonation in hardened cement pastes, Cem. Concr. Res. 123 (2019) 105795.
[24] H. Ma, Mercury intrusion porosimetry in concrete technology: tips in measurement, pore structure parameter acquisition and application, J. Porous. Mater. 21 (2014) 207–215.
[25] Y. Zhang, E. Schlangen, O. Çopuroğlu, Effect of slags of different origins and the role of sulfur in slag on the hydration characteristics of cement-slag systems, Constr. Build. Mater. 316 (2022) 125266.
[26] Y. Zhang, M. Liang, Y. Gan, et al., Effect of MgO content on the quantitative role of hydrotalcite-like phase in a cement-slag system during carbonation, Cem. Concr. Compos. 134 (2022) 104765.
[27] V. Ngala, C. Page, Effects of carbonation on pore structure and diffusional properties of hydrated cement pastes, Cem. Concr. Res. 27 (7) (1997) 995–1007.
[28] P.H.R. Borges, J.O. Costa, N.B. Milestone, et al., Carbonation of CH and C–S–H in composite cement pastes containing high amounts of BFS, Cem. Concr. Res. 40 (2) (2010) 284–292.
[29] M. Frías, S. Goñi, Accelerated carbonation effect on behaviour of ternary Portland cements, Compos. Part B Eng. 48 (2013) 122–128.
[30] Y. Zhang, M. Liang, Y. Gan, et al., Micro-mechanical properties of slag rim formed in cement–slag system evaluated by nanoindentation combined with SEM, Materials 15 (18) (2022) 6347.
[31] Y. Zhang, O. Çopuroğlu, The role of hydrotalcite-like phase and monosulfate in slag cement paste during atmospheric and accelerated carbonation, Cem. Concr. Compos. 132 (2022) 104642.
[32] F. Georget, B. Lothenbach, W. Wilson, et al., Stability of hemicarbonate under cement paste-like conditions, Cem. Concr. Res. 153 (2022) 106692.
[33] N. Doebelin, R. Kleeberg, Profex: a graphical user interface for the Rietveld refinement program BGMN, J. Appl. Crystallogr. 48 (5) (2015) 1573–1580.
[34] G.W. Groves, A. Brough, Ian G. Richardson, et al., Progressive changes in the structure of hardened C_3S cement pastes due to carbonation, J. Am. Ceram. Soc. 74 (11) (1991) 2891–2896.
[35] J. Ibáñez, L. Artús, R. Cuscó, et al., Hydration and carbonation of monoclinic C_2S and C_3S studied by Raman spectroscopy, J. Raman Spectrosc. 38 (1) (2007) 61–67.
[36] G. Villain, M. Thiery, G. Platret, Measurement methods of carbonation profiles in concrete: Thermogravimetry, chemical analysis and gammadensimetry, Cem. Concr. Res. 37 (8) (2007) 1182–1192.
[37] M. Thiery, G. Villain, P. Dangla, et al., Investigation of the carbonation front shape on cementitious materials: effects of the chemical kinetics, Cem. Concr. Res. 37 (7) (2007) 1047–1058.
[38] A. Morandeau, M. Thiery, P. Dangla, Investigation of the carbonation mechanism of CH and CSH in terms of kinetics, microstructure changes and moisture properties, Cem. Concr. Res. 56 (2014) 153–170.
[39] G.G. Litvan, Variability of the nitrogen surface area of hydrated cement paste, Cem. Concr. Res. 6 (1) (1976) 139–143.
[40] P. Sahoo, S. Ishihara, K. Yamada, et al., Rapid exchange between atmospheric CO_2 and carbonate anion intercalated within magnesium rich layered double hydroxide, ACS Appl. Mater. Interfaces 6 (20) (2014) 18352–18359.
[41] I. Richardson, Tobermorite/jennite-and tobermorite/calcium hydroxide-based models for the structure of CSH: applicability to hardened pastes of tricalcium silicate, β-dicalcium silicate, Portland cement, and blends of Portland cement with blast-furnace slag, metakaolin, or silica fume, Cem. Concr. Res. 34 (9) (2004) 1733–1777.
[42] J.C.A.A. Roelofs, J.A. van Bokhoven, A.J. van Dillen, et al., The thermal decomposition of Mg–Al hydrotalcites: effects of interlayer anions and characteristics of the final structure, Chem.–Eur. J. 8 (24) (2002) 5571–5579.
[43] J.T. Kloprogge, J. Kristófb, R.L. Frosta, Thermogravimetric analysis-mass spectrometry (TGA-MS) of hydrotalcites containing CO_3^{2-}, NO_3^-, Cl^-, SO_4^{2-} or ClO_4^-, Clay Odyssey 1 (2001) 451.
[44] V. Kocaba, E. Gallucci, K.L. Scrivener, Methods for determination of degree of reaction of slag in blended cement pastes, Cem. Concr. Res. 42 (3) (2012) 511–525.
[45] G. Rimmelé, V. Barlet-Gouédard, O. Porcherie, et al., Heterogeneous porosity distribution in Portland cement exposed to CO_2-rich fluids, Cem. Concr. Res. 38 (8–9) (2008) 1038–1048.
[46] M. Lesti, C. Tiemeyer, J. Plank, CO_2 stability of Portland cement based well cementing systems for use on carbon capture & storage (CCS) wells, Cem. Concr. Res. 45 (2013) 45–54.
[47] Y.J. Jeong, K.S. Youm, T.S. Yun, Effect of nano-silica and curing conditions on the reaction rate of class G well cement exposed to geological CO_2-sequestration conditions, Cem. Concr. Res. 109 (2018) 208–216.
[48] F. Georget, W. Soja, K.L. Scrivener, Characteristic lengths of the carbonation front in naturally carbonated cement pastes: implications for reactive transport models, Cem. Concr. Res. 134 (2020) 106080.
[49] Y. Yue, J. Wang, P.A. Muhammed Basheer, et al., A raman spectroscopy based optical fibre system for detecting carbonation profile of cementitious materials, Sensors Actuators B Chem. 257 (2018) 635–649.
[50] K. De Weerdt, G. Plusquellec, A. Belda Revert, et al., Effect of carbonation on the pore solution of mortar, Cem. Concr. Res. 118 (2019) 38–56.